The importance of future urban development in hourly extreme rainfall projections- comparing global warming and urbanization forcing over the Pearl River Delta region

Chenxi Hu
Chinese University of Hong Kong
Chi-Yung Tam (Francis.Tam@cuhk.edu.hk)
Chinese University of Hong Kong
Xinwei Li
University of Hong Kong
Kangning Huang
National Center for Atmospheric Research
Chao Ren
University of Hong Kong
Kwun Yip Fung
The University of Texas at Austin
Ziqian Wang
Sun Yat-sen University

Research Article

Keywords: urban development, global warming, Pearl River Delta (PRD), General Circulation Model (GCM) outputs, Weather Research and Forecasting Model (WRF)

Posted Date: June 23rd, 2021

DOI: https://doi.org/10.21203/rs.3.rs-622932/v1

Abstract

The impacts of future urban development and global warming forcing on hourly extreme rainfall over the Pearl River Delta (PRD) area have been investigated, by dynamically downscaling General Circulation Model (GCM) outputs using the Weather Research and Forecasting Model (WRF) at convection-permitting resolution, coupled with an Urban Canopy Model (UCM). Three downscaling experiments corresponding to different urban land cover (1999 and projected 2030) and climate (1951-to-2000 and 2001-to-2050 GCM simulations) were designed. Near-future climate change (up to 2050) and 1999-to-2030 urban development effects on PRD extreme precipitation were then examined. Results show that climate change and rapid urban development forcing have comparable positive effects on the intensity as well as heavy hourly rainfall probability over the PRD megacity. Global warming tends to increase heavy rainfall probability (from 40 to 60mm/hr) by about 1.3 to 1.8 times, but suppresses the frequency of light rainfall. Urban development increases urban rainfall probability within the whole range of intensity, with frequency for very heavy rainfall (> 90mm/hr) almost doubled. Overall, forcing due to rapid urban development plays an important role for projecting rainfall characteristic over the highly urbanized coastal PRD megacity, with impacts that can be comparable to global warming in the near future.

Introduction

There is now ample evidence that anthropogenic activities can exacerbate meteorological hazards such as heat waves and extreme rainfall. Since the last century, many places have seen rapid urbanization[1], which modulates climate over cities, leading to changes in surface high temperature[2,3], precipitation[4,5] and circulation[6,7]. It is well known that over the city area, more shortwave radiation is absorbed, due to modified land use, lower surface albedo and urban morphology[8]. Anthropogenic heat (AH) released from buildings, traffic and human populations can also promote the formation of urban heat island (UHI)[9], which also results in higher temperature[2] and provides an environment conductive to convection[10,11]. Many studies show that urbanization can enhance rainfall intensity downstream of some cities[12–15]. However, this result might depend on the UHI intensity; recent studies for Beijing demonstrate that strong UHI can increase rainfall directly over the downtown area, while during weak UHI days, precipitation tends to be bifurcated and avoids the city center[16,17]. AH released over megacities also plays a role in intensifying extreme rainfall and local convection[18–21]. On the other hand, impervious surface within a city means less water permeability and surface evaporation, which results in lower surface moisture and decreased latent heat flux to the atmosphere[22,23]. Studies show that decreased water content can reduce convective available potential energy (CAPE), hence the total precipitation amount over the Beijing urban area[24,25]. For coastal urban locales, enhanced surface temperature induced by urbanization can lead to stronger low-level flow from the ocean, which carries water vapor to the urban area. This is also conducive to stronger extreme precipitation intensity in some coastal cities such as Tokyo, Osaka, and the Pearl River Delta (PRD) megacity[20,21,26–30].

At the same time, climate change induced by anthropogenic emissions increases temperature strongly on the global scale[31], with some climate projections giving even stronger warming trends in the future[32]. Global warming is likely to suppress light precipitation over the monsoon area and contiguous US[33–35] or even total precipitation in some subtropical area such as Japan[36,37], due to enhanced thermal stability. On the other hand, according to the Clausius-Clapeyron (CC) relationship, the saturated vapor pressure increases by ~ 7% per degree near-surface warming, which means the atmosphere can accommodate more water vapor under a warmer climate background. The atmosphere will get moister in the future, and heavy rainfall will become stronger and more frequent[34,38,39]. Indeed, increasing trends of extreme rainfall have already been observed in many regions[40–42]. Studies using numerical simulations to examine the relationship between global warming and extreme rainfall also give results consistent with observations, with changes in the intensity of extreme rainfall generally exceeding those in the annual mean in the tropical areas[20,43,44].

The PRD region is a megacity cluster located in the southern coast of China, and has experienced rapid urbanization since the early 1980s; there is strong precipitation during the summer monsoon season, mainly due to severe thunderstorm systems and also tropical cyclones[45,46]. Observations indicate that both the intensity and frequency of PRD extreme rainfall have increased (more than 5% per decade) over most PRD megacity from 1971 to 2016[47], concurrent with regional urban expansion[28]. There is in fact robust intensification of summertime extreme rainfall by the UHI effect for all rainfall types in the PRD urban area[48]. At the same time, an increasing trend of both the strength and frequency of extreme rainfall can be observed over South China and PRD, while at the same time the number of rainy days has decreased significantly[32,49,50]. Results from numerical modeling also show that global warming can strongly enhance both intensity and frequency of extreme rainfall over PRD[20].

In this work, we investigate: (1) how urban development and global warming together might affect the characteristics of intense precipitation over PRD in the coming decades, and (2) whether the effect of urban development and climate change on PRD urban extreme rainfall are comparable. A recent work utilized a high-resolution model, with various types of urban land use incorporated, for assessing the impacts of both urban development and global warming on thermal comfort within PRD[51]. To our knowledge, this is the first study using a similar approach to exam their twin impacts on PRD extreme rainfall. In particular, dynamical downscaling of General Circulation Model (GCM) outputs, from historical runs and near-future climate projections, were carried out using a convection-permitting regional model with simulated urban canopy over city areas. Moreover, a predicted 2030 land use dataset over the PRD region is considered, which is derived from a land use prediction model that adopts with “training” based on historical PRD land use[52]. This way, magnitudes of extreme rainfall changes induced by anthropogenic activities (urban development and climate change) over the PRD region can be quantified; results based on similar modeling strategies can serve as a scientific basis for local policy makers to develop climate change adaptation plans in relation to the hydroclimate projections.

Results

In this study, three sets of parallel experiments were carried out: dynamical downscaling with 1999 urban land use under present climate (1951–2000) conditions (referred to as 99LS-HIS), dynamical downscaling with 1999 urban land use under near-future (2001–2050) climate conditions (referred to as 99LS-FUT), and finally dynamical downscaling with 2030 urban land use under near-future climate conditions (referred to as 30LS-FUT). Details of the experimental setup and land surface data prescriptions are given in methodology. We first investigate the change of surface temperature induced by urban development from 1999 to 2030 over the PRD area, as well as that due to global warming over a comparable period. Figure 2a compares the hourly 2-m temperature probability density function (PDF) in the range of 17 to 37^{o}C, based on data aggregated over the PRD urban locations, from the 99LS-HIS, 99LS-FUT, and 30LS-FUT runs. Comparing 99LS-FUT and 99LS-HIS, global warming enhances the 2-m temperature substantially in the urban area, and the frequency of high temperature increases for values larger than 27^{o}C. For instance, the likelihood in the range of 28-29^{o}C increases from 10–13%, and the location of maximum PDF shifted to higher values (from 26-27^{o}C to 27-28^{o}C) in the near future, meaning that the probability of higher temperature increases over the urban area under the near-future climate. At the same time, urbanization can also lead to a warmer city environment. Comparing the 30LS-FUT and 99LS-FUT results, the probability of high temperature is further increased due to urban development, with the strongest increment found in the range of 28-30^{o}C (with probability enhancement from 13–15%). Also shown in Fig. 2 gives the 30LS-FUT minus 99LS-HIS, and 30LS-FUT minus 99LS-FUT 2-m temperature, averaged over all extreme cases, in the PRD region. Overall, urban development can lead to surface warming by about 0.6 to 0.8^{o}C over the city area. When the effect of global warming is also considered, the 2-m temperature is enhanced by about 1^{o}C in the same region, as compared to 0.6^{o}C increase over the ocean. Therefore, according to these experiments, global warming and urban development can result in a comparable temperature increase over the PRD mega-urban region in the near future.

In order to investigate the influence of urban development and climate change on rainfall characteristics, Fig. 3 shows the mean rainfall difference between (a) 30LS-FUT and 99LS-HIS, and that between (b)30LS-FUT and 99LS-FUT, averaged over on all extreme cases considered. In the near future, the mean rainfall amount over the PRD urban area, for these extreme events, is enhanced by about 5–8 mm/day over part of the land area due to global warming, but the difference of rainfall intensity can be small in the coastal area. Future projected urban development also leads to more accumulated rainfall, but only at highly urbanized locations (the PRD city cluster comprising Guangzhou, Foshan, and Dongguan, between 113.2 to 113.7^{o}E, 22.8 to 23.3^{o}N; see open green circles in Fig. 3b), with significant enhancement by about 8–10 mm/day. Over the more southern part of the domain, rainfall change seems to be insignificant, which might be related to the weaker change of temperature and vertical motion in the southern part. When considering the whole 2030 PRD urban area, the area averaged accumulated rainfall increased by about 13.5% due to global warming; on the other hand, the increment is about 9.7% due to projected urban development alone. Statistical tests confirm that aforementioned precipitation change

over land in the northeast/west part of the domain, due to global warming in near future, passes the 95% significance level. Increased total rainfall in north and northwest part of the megacity area, caused by projected urban development, is also found to be statistically significant. Moreover, for the rainfall frequency, PDFs of hourly precipitation rates over the mega-urban area are considered. Figure 3c shows rainfall PDFs from 99LS-HIS, 99LS-FUT, and 30LS-FUT experiments within the range of 1 to 110mm/hr. Compared with 99LS-HIS, frequency of light rainfall events (those from 1 to 10mm/hr) for 99LS-FUT is decreased (by about 20% or more). On the other hand, global warming can strongly increase the probability of heavy rainfall (more than 50mm/hr) in the near future, with the likelihood enhanced by ~ 30 to 80%. By comparing 99LS-FUT and 30LS-FUT, it can be inferred that urban development can also increase the frequency of urban precipitation; such enhancement, however, is found for all rain rates (1-110mm/hr), with even stronger effect on heavy rainfall (i.e., rain rate more than 50mm/hr). For hourly rainfall in the range of 50-100mm/hr, the frequency increase is ~ 40 to 80% due to PRD urban development. It is noteworthy that both urban development and global warming can enhance the frequency and intensity of extreme rainfall over the PRD urban area.

To better compare impacts of urban development and global warming on rainfall frequency, Fig. 3d shows the ratio of rainfall probability between 30LS-FUT and 99LS-HIS (black), 99LS-FUT and 99LS-HIS (blue), and 30LS-FUT and 99LS-FUT (red) over the region with strongest signals in the Pearl River Estuary area (see black box in Figs. 3a and 3b). When considering both effects (see 30LS-FUT vs 99LS-HIS curve), it is obvious that frequency of heavy rainfall occurrence is enhanced more than that of light rainfall. It is noteworthy that urban development seems to have stronger influence on extremely heavy rainfall; the frequency of larger then 90mm/hr precipitation is doubled due to urban development (see 30LS-FUT vs 99LS-FUT). On the other hand, the downscaled global warming effect is most prominent within the range of 40-60mm/hr, with frequency enhanced by ~ 80 to 100% (see 99LS-FUT vs 99LS-FUT).

Under a warmer climate, there is higher surface evaporation (see Figure S1) which can increase the background moisture content. In fact, the precipitable water is increased in 99LS-FUT compared with 99LS-HIS in the whole PRD region (Figure S2), which is conducive to stronger extreme rainfall in the near future. However, the temperature and relative humidity difference caused by warmer background climate (99LS-FUT vs 99LS-HIS) increases with height, while the average temperature (relative humidity) difference over the urban area is only about 0.4^{o}C (0.57%) at surface, then increasing to 0.75^{o}C (1.04%) at 2000m (figure not shown). Hence, the 99LS-FUT experiment gives higher environment virtual temperature, leading to increased CIN for air parcels under 1400m compared to 99LS-HIS (see Figure S3). This is consistent with the results that global warming can enhance the thermal stability, making atmosphere more stable, and convection more difficult to be triggered[33–37]. The increased precipitable water and atmospheric stability plays an opposite effect on extreme rainfall. For these extreme precipitation events, more intense and frequent extreme rainfall over land area could be due to enhanced moisture content under a warmer climate, while the higher CIN is likely the reason why the frequency of light rainfall (1 to 10mm/hr) is suppressed in the PRD mega-urban area due to climate change.

It is known that urbanization results in lower surface humidity over the urban area due to decreased surface evaporation, which leads to a decrease of convective available potential energy (CAPE) for parcel under 600m of height. However, the CAPE difference is still weak above 600m (no more than 3J/kg) over the 2030 PRD megacity (figure not shown). Considering that the impact of urban development is not uniform over the whole city area, difference in CAPE for parcels rising at 1000m between 30LS-FUT and 99LS-FUT is calculated (see Figure S4). There is an increase of CAPE of about 15 to 30 J/kg over north and northwest part of the mega urban region (again locations with the greatest urban development, such as Guangzhou, Dongguan, Foshan, and Panyu, indicated by pen green circles in Figure S4), which strengthen local convection on these locations; enhanced CAPE is also consistent with the rainfall increase (about 3-12mm/d) at the same locations. To find out whether convection and local water vapor content are changed due to urban development, Fig. 4 gives the vertical profiles of specific humidity and wind difference between 30LS-FUT and 99LS-FUT, along a northeast-southwest cross section (see Fig. 1c). Red and blue bars, at the bottom of the same figure, indicate the projected new urban area in 2030, and existing urban area in 1999, respectively. Due to urban development, more water vapor is found at the height from 300m to 6km, which can be attributed to increased moisture convergence in relation to induced circulation by a stronger UHI effect, especially in the highly urbanized megacity area (such as Dongguan), with specific humidity increased more than 0.15g/kg from 500m to 5km. Compared with 99LS-FUT experiment, 30LS-FUT gives stronger vertical motion over the most urban area from 1km to 6km. This is especially the case over the highly urbanized region of 113.2 to 114.2^{o}E, with obvious development in 2030 compared to 1999. Similar results were found for other cross-sectional plots. For the east-west cross-section through Guangzhou (see Figure S5a), enhanced specific humidity and vertical motion were seen over the Guangzhou and Foshan area, and the anomalous specific humidity can reach 4km in the highly urbanized area; this is consistent with stronger vertical motion there. As can be inferred from the south-to-north cross-section through Guangzhou (see Figure S5c), urban development and presumably the induced additional UHI can lead to anomalous low-level southerly flow from the ocean towards to the city area, thus advecting moisture into the mega-urban region. Moreover, compared with PRD urban land use in 1999 and 2030, large changes of urban development were found in two regions between 22.9-23.2N, 113.0-113.4E (Guangzhou and Foshan) and 22.5-22.8N, 113.8-114.3E (Shenzhen and Hong Kong) (see Fig. 1b and 1c), while enhanced precipitation and CAPE were only found in former region due to urban development. For the latter region, there are also stronger low-level southerly flow and slightly enhanced water vapor above 500m due to urban development (see Figure S5e). However, the change of vertical wind speed are weak over the Hong Kong and Shenzhen; there are even decreased vertical wind speed above 3km over 22.6-22.8N due to urban development. It appears that due to the strongly enhanced vertical motion over Guangzhou, Foshan, and Dongguan, the sinking branch from the north and northwest part of the domain tends to suppress convection over other urban locations (such as Shenzhen and Hong Kong, 22.5-22.8N, 113.8-114.3E). Hence stronger convection and precipitation are only found in the north and northwest part of the megacity. Overall, for the 30LS-FUT experiment, stronger convection found over the area with strongest urban development is consistent with higher CAPE over the same locations; induced low-level convergence and southerly flow from the ocean act to increase the

atmospheric moisture content, which is also conducive to stronger and more frequent extreme rainfall there.

Discussions And Summary

In this study, impact of future urban development on hourly extreme rainfall projection over the PRD mega-urban region has been investigated and compared with global warming effect, based on dynamical downscaling of extreme rainfall cases taken from GCM runs using a convection-permitting regional model, with three types of urban land use and corresponding parameters incorporated in the model's urban canopy. Parallel experiments were designed by varying the urban land use (1999 vs 2030) and background climate conditions (present vs near-future). Results showed that urban development can lead to surface warming by about 0.6 to 0.8^{o}C over the city area. Near-future global warming effects can enhance surface temperature by ~ 0.3 to 0.8^{o}C (0.4 to 0.8^{o}C) over the PRD land (nearby ocean). For precipitation, both urban development and global warming can enhance the intensity as well as the occurrence rate of extreme rainfall. Global warming can increase the extreme rainfall amount (averaged over entire integrations for all selected extreme cases) over part of the PRD land area by about 3-12mm/day, while the increase due to urban development was found to be around 6-12mm/day over the north and northwest part of PRD region (i.e. locations which are projected to become even more urbanized in the near future). Moreover, the intensity of accumulated rainfall averaged over the 2030 PRD urban area increased by about 13.5% (9.7%) due to global warming (urban development). This result is consistent with a recent meta-data analysis which reported that accumulated rainfall increases by about 11 to 21% in the city center (and 14 to 22% in the downwind direction) due to urbanization[53]. According to the CC relationship, the saturated vapor pressure increases by ~ 7% per degree warming in low-level temperature. The GCM runs considered give 1.1^{o}C warming from 1951–2000 to 2001–2050, while the 95th percentile of daily rainfall intensity increases by about 7.4% over PRD (figures not shown). Similar scaling is found (approximately 7.9%/^{o}C warming) in our dynamical-downscaling results, when comparing 99LS-FUT vs 99LS-HIS domain averaged 95th percentile hourly rainfall for all cases.

It was also found that, due to the multi-center nature of PRD, sinking branch from the highly urbanized area could suppress convection over the urban in coastal areas (such as Shenzhen). Hence stronger convection and precipitation was only found in north and northwest part of the domain. Also noteworthy is that global warming has a negative impact on the frequency of light rainfall (by around 20% of reduction) during these extreme precipitation events, which may be attributed to stronger CIN, and more stable atmosphere under a warmer climate. But for heavy rainfall (within the range of 40 to 60mm/hr), global warming would substantially enhance its probability by about 1.3 to 1.8 times, which is supported by the enhanced evaporation and water vapor in the atmosphere under a warmer climate. Urban development, on the other hand, can increase the likelihood of urban rainfall in all ranges (1-110mm/hr). Fractional increase of probability from 99LS-FUT to 30LS-FUT is no more than 5% for light rainfall (1-10mm/hr), but reaching 40 to 80% for heavy rainfall (50-110mm/hr), and especially extremely heavy rainfall (stronger than 90 mm/hr). Significant enhancement of extreme rain rates is due to regionally

increased CAPE as well as decrease of CIN. The ocean also has an important effect versus urbanization on rainfall in the coastal PRD region; though urban development can reduce near-surface water vapor content in the large scale (30LS-FUT vs 99LS-FUT), due to stronger induced low-level southerly flow (from the ocean to megacity area) and stronger moisture flux convergence, urban development still results in more water vapor above the height of 300m, during extreme rainfall events. Overall, it is found that incorporating future urban development information is of great importance for the PRD region, in view of comparable impacts on temperature, intensity and frequency of extreme rainfall over the PRD mega-urban area compared to global warming forcing in the near future.

There are some limitations in this study. It is known that urban-induced aerosol can play a cooling effect and inhibit the formation of rainfall in some situations. However, aerosols and their future changes are not considered due to lack of data; their impacts on urban extreme rainfall will be researched in future studies. Moreover, extreme rainfall cases from only one GCM (namely the GFDL-ESM2M; see methodology) were examined in this study. For urban development, however, we suspect that its effect is not too sensitive to the background climate. Higher surface temperature and more moisture flux convergence induced by urban development can still enhance the intensity and frequency of precipitation over the PRD mega-urban area, under other GCM climate conditions. For global warming signals, further inspection showed that the increase of SST and evaporation given by this GCM are generally consistent with other GCM projections. Still, it will be of interest to dynamically downscale products from other GCMs, using the same regional modeling framework, to further compare the impacts of urbanization vs global warming on severe rainfall over PRD or other coastal megacities.

Finally, the urban canopy model used here can incorporate three types of urban land use only. Such representation might still not be realistic enough for a complex urban environment, such as that of the PRD mega-urban cluster. Details such as heat released by air conditioning and its timing, interaction with various atmospheric layers, etc., are neglected. In our next study, we plan to adopt a multi-layer urban canopy module that also allows more urban land types, with parameters based on the World Urban Database and Access Portal Tools (WUDAPT) dataset[54,55]. Such a modeling system will be ideal for studying the interaction between realistic urban environment and meso-scale systems. Results should be invaluable for mitigation of and adaptation to extreme weather and related hazards happening in highly urbanized locales, such as urban flooding (compounded by the effect of impervious surfaces[56]), under the present as well as the future climate.

Methodology

Data description and model evaluation

The Weather Research and Forecasting (WRF) model version 3.8.1 with the Advanced Research WRF dynamic core[57] coupled with the single-layer urban canopy model (SLUCM)[58], was used to dynamical downscale extreme precipitation events over the PRD area, as identified from the Geophysical Fluid Dynamical Laboratory Earth System model version 2 (GFDL-ESM2M[59,60]) historical run (1950–2005) and

the RCP8.5 projection (2006–2050). The GFDL-ESM2M atmospheric component has a horizontal resolution of 2^o x 2.5^o in latitudes and longitudes, respectively, and its ocean component is the Modular Ocean Model version 4 (MOM4). The model gives reasonable performance in simulating the East Asia monsoon circulation[61]. Fung et al[20] compared model products including temperature (Ta), geopotential height (H), U-wind (Ua) and V-wind (Va) were compared with their counterparts from the ERA-Interim reanalysis data[62]. Figure S6 shows the monthly mean values of the temperature, geopotential height, U-wind, and V-wind variables from GFDL-ESM2M versus those from ERA-interim, for the months of May, June, July, August, and September, for the 1970–2014 period; climatological summertime (May-to-September) mean distribution of 500hPa temperature, 500 hPa geopotential height, and 850 hPa temperature with u,v wind circulation are shown in Figure S7. GFDL-ESM2M systematically underestimates the near-surface (mid-tropospheric) temperature by about 1K. U-wind and v-wind are simulated well throughout the whole troposphere. Features such as the western Pacific subtropical high and the monsoon circulation from equator to the South China Sea are also captured, as seen reflected by the 850 hPa wind field. Taylor diagrams are used to describe their pattern correction and RMSE (Figure not shown). The GFDL-ESM2M can simulate well the temperature, geopotential height, u-wind and v-wind (with correlation coefficient $>$ 0.8 and standardized deviation of 0.6–1.4) in the summer period over the East Asia region. Precipitation in GFDL-ESM2M is also assessed by comparing model summertime mean rainfall from 1951 to 2007 with the station-based APHRODITE land precipitation data (see Figure S8). The model can reproduce major features well in East Asia such as heavy rainfall in south Tibet Plateau and over the Southeast Asia, and performs well in South China. Overall, the GFDL-ESM2M outputs give reasonable performance in atmospheric parameters over the East Asia area.

WRF setting and extreme case selection

Physical parameterizations in WRF include the use of the NOAH Land Surface Model (LSM) (for supporting SLUCM in the model environment[63,64], the Rapid Radiative Transfer Model for General Circulation Model (RRTMG) for longwave radiation[65], the short wave radiation scheme by Dudhia[66], the WRF single-moment 6-class microphysics scheme[67], Eta similarity theory for surface layer options[68], the Bougeault-Lacarrere planetary boundary layer scheme[69], and the simplified Arakawa-Schubert (SAS) GFS cumulus parameterization[70] (for the outermost domain only). Figure 1a shows the nested domains for the downscaling experiments, which cover East Asia/western north Pacific (2.23-43.82^{o}N, 70.81-147.05^{o}E, at 50km x 50km resolution), South China (19.94-27.09^{o}N, 110.68-117.60^{o}E, at 10km x 10km resolution) and PRD (21.5-23.83^{o}N, 112.51-115.04^{o}E, at 2km x 2km resolution). There were 39 vertical levels, reaching the height of ~ 10hPa.

Moreover, extreme rainfall events were taken from the historical as well as RCP8.5 simulations of GFDL-ESM2M. Daily mean precipitation averaged over the land area of South China region (17-27^{o}N, 105-117^{o}E) was first computed. Days during which the daily rainfall is larger than the 99th percentile (based on rainfall on wet days, when rain rate > 0.1mm/day) were defined as extreme rain days. 60 extreme cases in the summertime period of May to September, not related to tropical cyclone (TC)-like systems

(hereinafter referred to as non-TC cases) were selected. 30 extreme cases were selected from the historical era (1951–2000), and 30 extreme cases from the near-future era (2001–2050). GCM outputs from these cases were then downscaled by WRF, with integrations starting from 48 hours prior to the extreme rain day and lasting for at least five days.

Local Climate Zone (LCZ) Data, UCM and Model Experiments

Altogether, three sets of downscaling experiments using WRF-SLUCM were conducted: in 99LS-HIS, extreme events from the GFDL-ESM2M present climate run (1951–2000) were dynamical downscaled, with prescribed 1999 urban land use; in 99LS-FUT, extreme rainfall cases from the near-future (2001–2050) run with 1999 urban land were downscaled; finally, in 30LS-FUT, the same sets of extreme rain cases as in 99LS-FU were downscaled, with 2030 urban land use information in SLUCM. For the highly urbanized PRD region, detailed land use/land cover change (LULCC) types in 1999 and the near-future projection in 2030 built on the WUDAPT protocol were developed[54,55] with a spatial resolution of 1km x 1km, and classified according to the local climate zone (LCZ) scheme[71]. LCZ classification includes ten types for urban land use (namely Compact High-Rise, Compact Mid-Rise, Compact Low-Rise, Open High-Rise, Open Mid-Rise, Open Low-Rise, Lightweight Low-Rise, Large Low-Rise, Sparsely Built, Heavy Industry), and seven types for natural land use (Dense Trees, Scattered Trees, Bush and Scrub, Low Plants, Bare Rock or Paved, Bare Soil or Sand, and Water). Each LCZ type has its own set of UCM parameters and attributes[72] (such as surface albedo, building height, sky view factor, etc.). Urban land use information of PRD in 1999 (the present era) and in 2030 (the projected near-future era) were prescribed differently in the model[55]. For the urban land use in 2030, the near future LCZ maps over the PRD region is projected by Huang[52], with a land-use land cover change (LULCC) model: the Geographical Simulation and Optimization System (GeoSOS) – Future Land Use Simulation (FLUS) model[73]. Firstly, a data mining technique, namely the Artificial Neural Network (ANN), is used to learn the occurrence probability for each land-use from historical LCZ maps, based on geographical factors such as slopes, and distance from city centers. Secondly, the future demands for urban land-use are projected based on trajectories of demographic and socioeconomic developments. Finally, the Cellular Automata (CA) model is used to model the land-uses conversions based on current LCZ maps (2014 LCZ maps), with the occurrence and neighborhood influence probability be repeated until the future demands are met. And the projected near-future maps are generated by the CA model.

To simplify the prediction scheme, the ten types of urban LCZ were regrouped into three types: “Low Intensity Residence” (type 1) comprises Open Mid Rise, Open Low Rise, Sparsely Built, Open High Rise, Lightweight Low Rise, Large Low Rise; “High Intensity Residence” (type 2) comprise Compact Mid Rise; Compact Low Rise, and finally, “Commercial and Industrial” (type 3) includes both Compact High Rise and Heavy Industry. Table 1 gives the UCM parameters prescribed for these three land use types. Also shown in Fig. 1 are the 1999 and 2030 urban land use distributions (after re-grouping) in the innermost

model domain, with yellow, red, and purple indicating type 1, type 2 and types 3 urban land use, respectively.

Table 1
Values of UCM parameters prescribed for three types of urban categories.

UCM parameter	Type1	Type2	Type3
Anthropogenic heat [W m^{-2}]	15.0	50.0	200.0
Building height [m]	13.31	14.01	53.92
Urban fraction	0.4	0.9	0.7
Standard Deviation of roof height [m]	10.42	5.64	33.18
Roof width [m]	38.01	14.28	35.5
Road width [m]	22.98	13.91	29.6
Surface albedo of road	0.2	0.17	0.18
Surface albedo of roof	0.142	0.165	0.115
Surface albedo of building wall	0.208	0.2	0.22

Declarations

Author Contribution

All authors contributed to designing the research, interpreting results and writing the manuscript. C.-Y. T. supervised the work. C. H. carried out the WRF model runs, analyzed the data and plotted the figures. C. H., Z. W., and C.-Y. T. prepared the main text. C. H., and K. F. provided the model evaluation of GFDL-ESM2M. X. L., C. R., and K. H. performed the 1999 and projected 2030 PRD land use data build on WUDAPT protocol and touched up the manuscript.

Additional Information

Competing financial interests: The authors declare no competing financial interests.

References

1. Hannah R., Urbanization. Published online at OurWorldInData.org. Retrieved from “https://ourworldindata.org/urbanization” (2018).
2. Mohajerani, A., Bakaric, J., and Jeffrey-Bailey, T., The urban heat island effect, its causes, and mitigation, with reference to the thermal properties of asphalt concrete. Journal of Environmental Management,197, 522-538 (2017).

3. Luo, M., and Lau, N.-C., Heat waves in southern China: Synoptic behavior, long-term change and urbanization effects, Journal of Climate, vol. 30 (2), 703-720 (2017).
4. Huff, F., and Changnon, S., Climatological Assessment of Urban Effects on Precipitation at St. Louis. Journal of Applied Meteorology, 11(5), 823-842 (1972).
5. Han, J., Baik, J., and Lee, H., Urban impacts on precipitation. Asia-Pacific Journal of Atmospheric Sciences, 50(1), 17-30 (2014).
6. Li, M., Song, Y., Mao, Z., Liu, M., and Huang, X., Impacts of thermal circulations induced by urbanization on ozone formation in the Pearl River Delta region, China. Atmospheric Environment, 127, 382-392 (2016).
7. Fan, Yifan, Li, Yuguo, & Yin, Shi. (2018). Interaction of multiple urban heat island circulations under idealised settings. Building and Environment, 134, 10-20.
8. Soltani, A., and Sharifi, E., Daily variation of urban heat island effect and its correlations to urban greenery: A case study of Adelaide. Frontiers of Architectural Research, 6(4), 529-538 (2017).
9. Shahmohamadi, P, Che-Ani, A. I, Maulud, K. N. A, Tawil, N. M, and Abdullah, N. A. G., The Impact of Anthropogenic Heat on Formation of Urban Heat Island and Energy Consumption Balance. Urban Studies Research, 2011, 1-9 (2011).
10. Baik, J., Kim, Y., and Chun, H., Dry and Moist Convection Forced by an Urban Heat Island. Journal of Applied Meteorology (1988), 40(8), 1462-1475 (2001).
11. Han, J., and Baik, J., A theoretical and numerical study of urban heat island-induced circulation and convection. Journal of the Atmospheric Sciences, 65(6), 1859-1877 (2008).
12. Changnon, S, The La Porte weather anomaly—fact or fiction? Bulletin of the American Meteorological Society, 49(1), 4-11 (1968).
13. Shepherd, J., and Burian, S., Detection of Urban-Induced Rainfall Anomalies in a Major Coastal City. Earth Interaction, 2003, Vol. 7 (2003).
14. Lin, C., Chen, W., Liu, S., Liou, Y., Liu, G., and Lin, T., Numerical study of the impact of urbanization on the precipitation over Taiwan. Atmospheric Environment, 42(13), 2934-2947 (2008).
15. Shem, W., and Shepherd, M., On the impact of urbanization on summertime thunderstorms in Atlanta: Two numerical model case studies. Atmospheric Research, 92(2), 172-189 (2009).
16. Dou, J., Wang, Y., Bornstein, R., and Miao, S., Observed Spatial Characteristics of Beijing Urban Climate Impacts on Summer Thunderstorms. Journal of Applied Meteorology and Climatology, 54(1), 94-105 (2015).
17. Zhang, Y., Miao, S., Dai, Y., and Bornstein, R., Numerical simulation of urban land surface effects on summer convective rainfall under different UHI intensity in Beijing. Journal of Geophysical Research: Atmospheres, 122(15), 7851-7868 (2017).
18. Holst, C. C., Tam, C., and Chan, J., Sensitivity of urban rainfall to anthropogenic heat flux: A numerical experiment. Geophysical Research Letters, 43(5), 2240-2248 (2016).

19. Holst, C., Chan, J., and C.-Y. Tam., Sensitivity of Precipitation Statistics to Urban Growth in a Subtropical Coastal Megacity Cluster. Journal of Environmental. Sciences, 59, 6-12 (2017).
20. Fung, K.Y., C.-Y. Tam, T.C. Lee and Z. Wang., Comparing the Anthropogenic Heat and Global Warming Impacts on Extreme Precipitation in urbanized Pearl River Delta area based on Dynamical Downscaling, Journal of Geophysical Research., submitted. (Preprint: https://doi.org/10.1002/essoar.10506761.1) (2021)
21. Hu, C., Fung, K., Tam, C-Y., Wang, Z., Urbanization impacts on Pearl River Delta extreme rainfall – sensitivity to land cover change vs anthropogenic heat. Earth and Space Science, (2021).
22. Bornstein, R., Observation of the Urban Heat Island Effect in New York City. Journal of Applied Meteorology (1968).
23. Oke, T., The urban energy balance. Progress in Physical Geography, 12(491) (1988).
24. Guo, X., Fu, D., and Wang, J., Mesoscale convective precipitation system modified by urbanization in Beijing city. Atmospheric Research., 82, 112-126 (2006).
25. Zhang, C., Chen, F., Miao, S., Li, Q., Xia, X., and Xuan, C., Impacts of urban expansion and future green planting on summer precipitation in the Beijing metropolitan area. Journal of Geophysical Research: Atmospheres., 114(D2) (2009).
26. Kusaka, H., Nawata, K., Suzuki-Parker, A., Takane, Y., and Furuhashi, N., Mechanism of Precipitation Increase with Urbanization in Tokyo as Revealed by Ensemble Climate Simulations. Journal of Applied Meteorology and Climatology, 53(4), 824-839 (2014).
27. Shimadera, H., Kondo, A., Shrestha, K., Kitaoka, K., and Inoue, Y., Numerical Evaluation of the Impact of Urbanization on Summertime Precipitation in Osaka, Japan. Advances in Meteorology, 2015(2015), 149-159 (2015).
28. Wang, D., Jiang, P., Wang, G., and Wang, D., Urban extent enhances extreme precipitation over the Pearl River Delta, China. Atmospheric Science Letters, 16(3), 310-317 (2015).
29. Xiao, Z., Wang, Z., Huang, M., Luo, X., Liang, Y., and Lin, Z., Urbanization in an underdeveloped city-Nanning, China and its impact on a heavy rainfall event in July. Earth and Space Science, 7, e2019EA000991 (2020).
30. Wen, J., Chen, J., Lin, W., Jiang, B., Xu, S., and Lan, J., Impacts of Anthropogenic Heat Flux and Urban Land-Use Change on Frontal Rainfall near Coastal Regions: A Case Study of a Rainstorm over the Pearl River Delta, South China. Journal of Applied Meteorology and Climatology, 59(3), 363-379 (2020).
31. Knutson, T. R., J. P. Kossin, C. Mears, et al. Detection and attribution of climate change. Climate Science Special Report: Fourth National Climate Assessment, Volume I, D. J. Wuebbles, D. W. Fahey, K. A. Hibbard, et al. Eds., U. S. Global Change Research Program, Washington, DC, USA, 114–132 (2017).
32. Meehl, G., Stocker, T., Collins, W., et al. Global Climate Projections. In: Climate Change 2007: The Physical Science Basis. Contribution of Working Group I to the Fourth Assessment Report of the Intergovernmental Panel on Climate Change [Solomon, S., D. Qin, M. Manning, Z. Chen, M. Marquis,

K.B. Averyt, M. Tignor and H.L. Miller (eds.)]. Cambridge University Press, Cambridge, United Kingdom and New York, NY, USA (2007).

33. Chou, C., Chen, C., Tan, P., and Chen, K., Mechanisms for global warming impacts on precipitation frequency and intensity. Journal of Climate, 25(9), 3291–3306 (2012).
34. Hsu, P., Li, T., Luo, J., Murakami, H., Kitoh, A., and Zhao, M., Increase of global monsoon area and precipitation under global warming: A robust signal? Geophysical Research Letters, 39(6) (2012).
35. Dai, A., Rasmussen, R., Liu, C., Ikeda, K., and Prein, A., A new mechanism for warm-season precipitation response to global warming based on convection-permitting simulations. Climate Dynamics, 55(1-2), 1-26 (2017).
36. Chou, C., and Neelin, J., Mechanisms of Global Warming Impacts on Regional Tropical Precipitation. Journal of Climate, 17(13), 2688-2701 (2004).
37. Kenshi, H., Izuru, T., Yasutaka, W., and Tomomichi, O., Physical responses of convective heavy rainfall to future warming condition: Case study of the hiroshima event. Frontiers in Earth Science (Lausanne), 2018-04-19, Vol.6 (2018).
38. Marta, M., and Jan, K., Overview of Observed Clausius-Clapeyron Scaling of Extreme Precipitation in Midlatitudes. Atmosphere, 11(8), 786 (2020).
39. Tabari, H., Climate change impact on flood and extreme precipitation increases with water availability. Scientific Reports, 10(1), 13768 (2020).
40. Iwashima, T., and Yamamoto, R., A statistical analysis of the extreme events: Long-term trend of heavy daily precipitation. Journal of the Meteorological Society of Japan, 71(5), 637-640 (1993).
41. Karl, T., and Knight, R., Secular trends of precipitation amount, frequency, and intensity in the USA. Bulletin of the American Meteorological Society, 79, 231-241 (1998).
42. Myhre, G, Alterskjaer, K, Stjern, C. W, Hodnebrog, O, Marelle, L, Samset, B. H, et al. Frequency of extreme precipitation increases extensively with event rareness under global warming. Scientific Reports, 9(1), 16063-10 (2019).
43. Chen, H., Projected change in extreme rainfall events in China by the end of the 21st century using CMIP5 models. Chinese Science Bulletin, 58(12), 1-10 (2013).
44. Kharin, V., Zwiers, F., Zhang, X., and Hegerl, G., Changes in temperature and precipitation extremes in the IPCC ensemble of global coupled model simulations. Journal of Climate, 20(8), 1419-1444 (2007).
45. Wai, M. K., Welsh, T., and Ma, W. M., The Timing and Distribution of Summer Convective Rainfall Over Hong Kong and South China, Hong Kong Meteorological Society Bulletin, 5(2) (1995).
46. Chang, C., Lei, Y., Sui, C., Lin, X., and Ren, F, Tropical cyclone and extreme rainfall trends in East Asian summer monsoon since mid-20th century. Geophysical Research Letters, 39(18) (2012).
47. Yan, Meng, Chan, Johnny C. L, and Zhao, Kun., Impacts of Urbanization on the Precipitation Characteristics in Guangdong Province, China. Advances in Atmospheric Sciences, 37(7), 696-706 (2020).

48. Wu, M., Y. Luo, F. Chen, and W. K. Wong., Observed Link of Extreme Hourly Precipitation Changes to Urbanization over Coastal South China. Journal of Applied Meteorology and Climatology., 58, 1799–1819 (2019).
49. Zhang, Q., Xu, C.-Y., Becker, S., Zhang, Z.X., Chen, Y.D. and Coulibaly, M., Trends and abrupt changes of precipitation maxima in the Pearl River basin, China. Atmospheric Science Letter., 10: 132-144 (2009).
50. Wong, M.C., Mok, H.Y. and Lee, T.C., Observed changes in extreme weather indices in Hong Kong. International Journal of Climatology., 31: 2300-2311 (2011).
51. Wang, Z., Z. Xiao, C.-Y. Tam, W. Pan, J. Chen. C. Hu, C. Ren, W. Wei and S. Yang., The projected effects of urbanization and climate change on summer thermal environment in Guangdong-Hong Kong-Macao Greater Bay Area of China, Urban Climate, 37, 2021, 100866 (2021).
52. Huang, K., Leng, J., Xu, Y., Li, X., Cai, M., Wang, R., and Ren, C., Facilitating Urban Climate Forecasts in Rapidly Urbanizing Regions with Land-use Change Modeling. Urban Climate, 36, 100806 (2021).
53. Liu, J., Niyogi, D., Meta-analysis of urbanization impact on rainfall modification Scientific Reports 9(1), 7301 (2019).
54. Ching, J., Mills, G., el al., WUDAPT: An Urban Weather, Climate, and Environmental Modeling Infrastructure for the Anthropocene: WUDAPT is an international community-generated urban canopy information and modeling infrastructure to facilitate urban-focused climate, weather, air quality, and energy-use modeling application studies. Bulletin of the American Meteorological Society, 99(9), 1907-1924 (2018).
55. Wang, R., Cai, M., Ren, C., Bechtel, B., Xu, Y., and Ng, E., Detecting multi-temporal land cover change and land surface temperature in Pearl River Delta by adopting local climate zone. Urban Climate, 28, 100455 (2019).
56. Blum, A., Ferraro, P., Archfield, S., Ryberg, K, Causal Effect of Impervious Cover on Annual Flood Magnitude for the United States Geophysical Research Letters 47(5) (2020).
57. Skamarock, W., Klemp, J., Dudhia, J., Gill, D., Barker, D., Duda, M., Huang, X., Wang, W., and Powers, J., A description of the advanced research WRF version 3 NCAR Tech. Note, NCAR/TN–475+STR (2008).
58. Kusaka, H., and Kimura, F., Thermal Effects of Urban Canyon Structure on the Nocturnal Heat Island: Numerical Experiment Using a Mesoscale Model Coupled with an Urban Canopy Model, Journal of Applied Meteorology, 43(12), 1899–1910 (2004).
59. Dunne, J., John, J., Adcroft, A., Griffies, S., Hallberg, R., Shevliakova, E., et al. GFDL's ESM2 Global Coupled Climate–Carbon Earth System Models. Part I Physical Formulation and Baseline Simulation Characteristics. Journal of Climate, 25(19), 6646-6665 (2012).
60. Dunne, J., Jasmin, G., John, E., Shevliakova, E., Ronald, J., et al. GFDL's ESM2 Global Coupled Climate-Carbon Earth System Models. Part II: Carbon System Formulation and Baseline Simulation Characteristics. Journal of Climate, 26(7), 2247-2267 (2013).

61. McSweeney, C. F., Jones, R. G., Lee, R. W., and Rowell, D. P., Selecting CMIP5 GCMs for downscaling over multiple regions, Climate Dynamics, 44(11–12), 3237–3260 (2015).
62. Dee, D., Uppala, S., Simmons, A., Berrisford, P., Poli, S., Kobayashi, U., et al. The ERA-Interim Reanalysis: Configuration and Performance of the Data Assimilation System. Quarterly Journal of The Royal Meteorological Society, 137(656), 553-597 (2011).
63. Chen, F., and Dudhia, J., Coupling and advanced land surface-hydrology model with the Penn State-NCAR MM5 modeling system. Part I: Model implementation and sensitivity. Monthly Weather Review, 129(4), 569-585 (2001).
64. Tewari, M. F., Chen, F., Kusaka, H., and Miao, S., Coupled WRF/Unified Noah/urban-canopy modeling system, NCAR WRF Documentation, NCAR, Boulder, 1–20 (2008).
65. Iacono, M., Delamere, J., Mlawer, E., Shephard, M., Clough, S., and Collins, W., Radiative forcing by long-lived greenhouse gases: Calculations with the AER radiative transfer models. Journal of Geophysical Research: Atmospheres, 113(D13) (2008).
66. Dudhia, J., Numerical study of convection observed during the Winter Monsoon Experiment using a mesoscale two-dimensional model. Journal of the Atmospheric Sciences, 46, 3077-3107 (1989).
67. Hong, S.-Y., and Lim, J.-O. J., The WRF single-moment 6-class microphysics scheme (WSM6), Journal of the Korean Meteorological Society, 42(2), 129–151 (2006).
68. Janjic, Z. I., Nonsingular implementation of the Mellor-Yamada Level 2.5 Scheme in the NCEP Meso model. NCEP Office Note No. 437, 61 pp (2002).
69. Bougeault, P., and Lacarrere, P, Parameterization of Orography-Induced Turbulence in a Mesobeta-Scale Model, Monthly Weather Review, 117, 1872-1890 (1989).
70. Han, J., and Pan, H., Revision of convection and vertical diffusion schemes in the NCEP Global Forecast System. Weather and Forecasting, 26(4), 520-533 (2011).
71. Stewart, I., Oke, T., Local Climate Zones for Urban Temperature Studies. Bulletin of the American Meteorological Society. 93, 1879–1900 (2012).
72. Stewart, I., Oke, T., Krayenhoff, E., Evaluation of the ‘local climate zone’ scheme using temperature observations and model simulations. International Journal of Climatology, 34 (4), 1062–1080 (2014).
73. Liu, X., Liang, X., Li, X., Xu, X., Ou, J., Chen, Y., Li, S., Wang, S., Pei, F, A future land use simulation model (FLUS) for simulating multiple land use scenarios by coupling human and natural effects. Landscape and Urban Planning 168, 94–116 (2017).

Figures

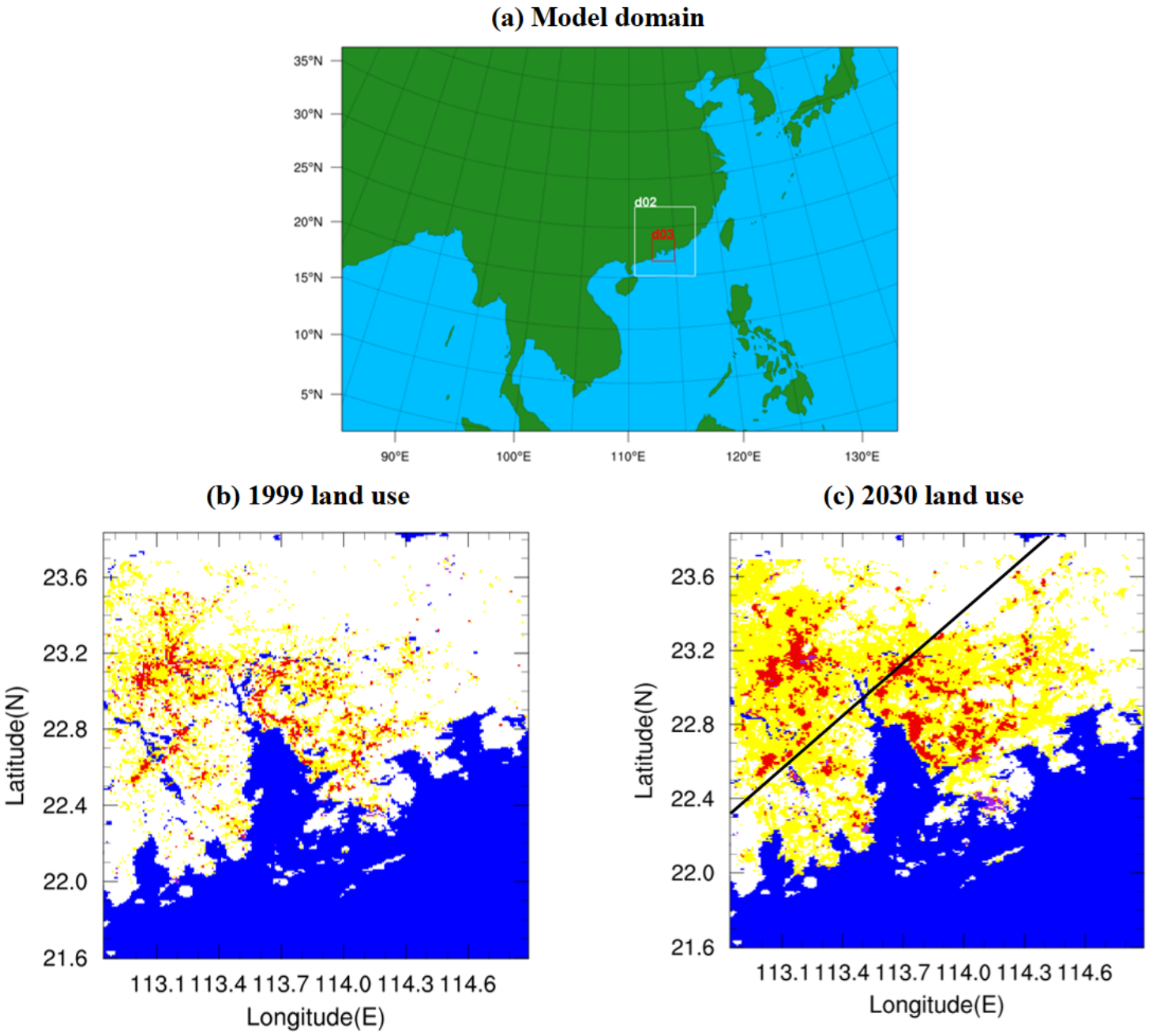

Figure 1

(a) Nested domains for the WRF simulations. (b) Land use categories of 1999 in the innermost domain with “Low Intensity Residence”, “High Intensity Residence”, and “Commercial and Industrial” locations indicated by yellow, red, and purple shading. Same as (b) but for projected 2030 urban land use. Black line indicates the cross-sectional plane for Figure 4.

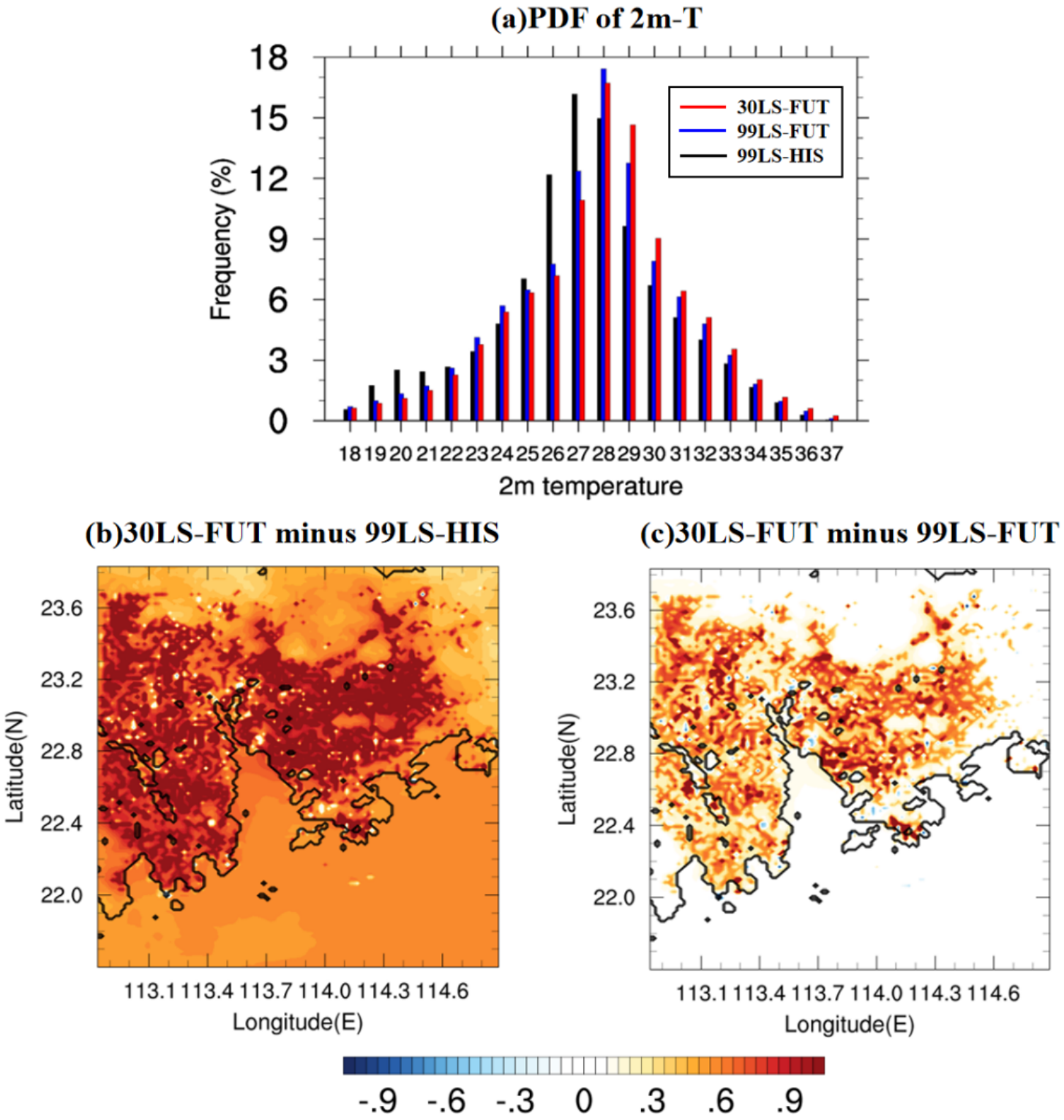

Figure 2

(a) PDFs of hourly 2m temperature within the range of 17-37oC for the 99LS-HIS (black), 99LS-FUT (blue), 30LS-FUT (red) experiments over corresponding urban locations within PRD (all urban grids in 1999 or 2030 land use). (b) 2m temperature difference (units:˚C) between (b) 99LS-HIS and 30LS-FUT and (c) 99LS-FUT and 30LS-FUT. Temperatures are computed by averaging over entire integrations for all selected extreme cases. See text for details. The coastline is shown by black line.

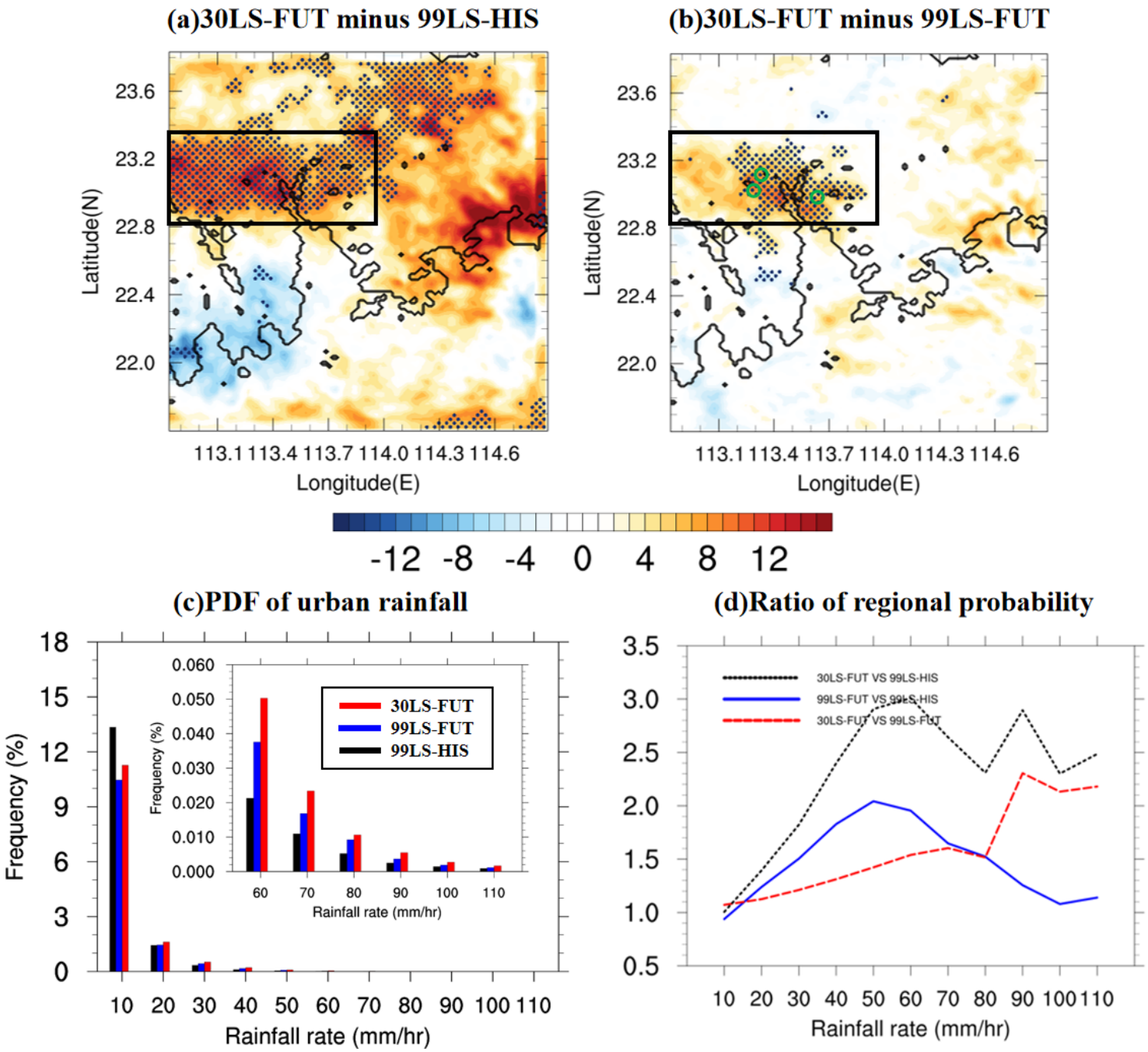

Figure 3

(a), (b) Same as Figures 2b, and 2c except for daily accumulated rainfall (units: mm/day), averaged over entire integrations for all selected extreme cases, with green circles indicating the locations, from west to east, of Foshan, Guangzhou, and Dongguan. Locations in which the difference exceeds the 95% significance level are denoted by black dots. (c) PDFs of hourly precipitation rates within the ranges of 1-10, 10-20, 20-30, 30-40, 40-50, 50-60, 60-70, 70-80, 80-90, 90-100, and 100-110 mm/hr (denoted by the labels 10, 20, 30, 40, 50, 60, 70, 80, 90, 100, 110mm/h, respectively) for the 99LS-HIS (black), 99LS-FUT (blue), 30LS-FUT (red) experiments over corresponding urban locations within PRD (i.e., all urban grids for 1999 or 2030 land use). (d) Ratio of hourly rain rate probability between 30LS-FUT and 99LS-HIS (black),

99LS-FUT and 99LS-HIS (blue), and 30LS-FUT and 99LS-FUT (red) within the ranges of 1-110mm/hr, based on hourly rainfall data within the black box region in Figures 3a and 3b.

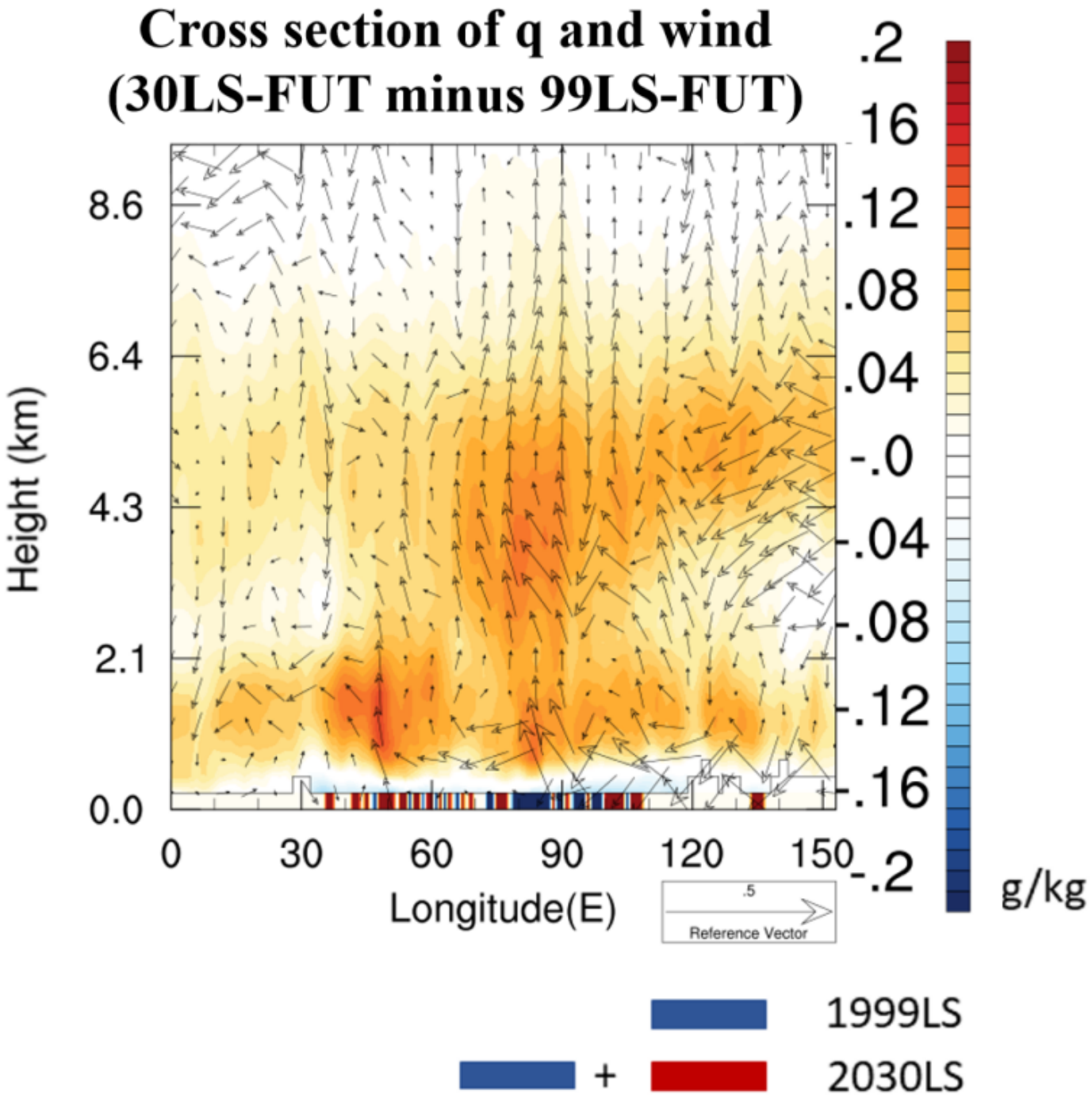

Figure 4

(a), (b) Same as Figures 2b, and 2c except for daily accumulated rainfall (units: mm/day), averaged over entire integrations for all selected extreme cases, with green circles indicating the locations, from west to east, of Foshan, Guangzhou, and Dongguan. Locations in which the difference exceeds the 95% significance level are denoted by black dots. (c) PDFs of hourly precipitation rates within the ranges of 1-10, 10-20, 20-30, 30-40, 40-50, 50-60, 60-70, 70-80, 80-90, 90-100, and 100-110 mm/hr (denoted by the

labels 10, 20, 30, 40, 50, 60, 70, 80, 90, 100, 110mm/h, respectively) for the 99LS-HIS (black), 99LS-FUT (blue), 30LS-FUT (red) experiments over corresponding urban locations within PRD (i.e., all urban grids for 1999 or 2030 land use). (d) Ratio of hourly rain rate probability between 30LS-FUT and 99LS-HIS (black), 99LS-FUT and 99LS-HIS (blue), and 30LS-FUT and 99LS-FUT (red) within the ranges of 1-110mm/hr, based on hourly rainfall data within the black box region in Figures 3a and 3b.

Supplementary Files

This is a list of supplementary files associated with this preprint. Click to download.

- SupplementaryMaterials.docx